Geophysical Journal International

Geophys. J. Int. (2023) **233,** 1429–1443
Advance Access publication 2022 December 24
GJI Heat Flow and Volcanology

https://doi.org/10.1093/gji/ggac517

Atmospheric and ionospheric waves induced by the Hunga eruption on 15 January 2022; Doppler sounding and infrasound

Jaroslav Chum,[1] Tereza Šindelářová,[1] Petra Koucká Knížová,[1] Kateřina Podolská,[1] Jan Rusz,[1] Jiří Baše,[1] Hiroyuki Nakata,[2] Keisuke Hosokawa,[3] Michael Danielides,[4] Carsten Schmidt,[5] Leon Knez,[5] Jann-Yenq Liu,[6] María Graciela Molina,[7,8] Mariano Fagre,[7] Zama Katamzi-Joseph,[9] Hiroyo Ohya,[2] Tatsuya Omori,[2] Jan Laštovička,[1] Dalia Obrazová Burešová,[1] Daniel Kouba,[1] Jaroslav Urbář[1] and Vladimír Truhlík[1]

[1]*Institute of Atmospheric Physics of the Czech Academy of Sciences, Prague* 14100, *Czech Republic. E-mail: jachu@ufa.cas.cz*
[2]*Chiba University, Chiba* 263-8522, *Japan*
[3]*The University of Electrocommunications, Tokyo* 182-8585, *Japan*
[4]*Danielides Space Science Consulting, Bentzin* 17129, *Germany*
[5]*DLR, Oberpfaffenhofen* 82234, *Germany*
[6]*National Central University, Zhongli* 32001, *Taiwan*
[7]*Universidad Nacional de Tucumán, T*4000, *Argentina*
[8]*Consejo Nacional de Investigaciones Científicas y Técnicas, CONICET, C*1425*FQB, Argentina*
[9]*South African National Space Agency, Hermanus* 7200, *South Africa*

Accepted 2022 December 23. Received 2022 December 21; in original form 2022 May 31

SUMMARY

The massive explosive eruption of the Hunga volcano on 15 January 2022 generated atmospheric waves that were recorded around the globe and affected the ionosphere. The paper focuses on observations of atmospheric waves in the troposphere and ionosphere in Europe, however, a comparison with observations in East Asia, South Africa and South America is also provided. Unlike most recent studies of waves in the ionosphere based on the detection of changes in the total electron content, this study builds on detection of ionospheric motions at specific altitudes using continuous Doppler sounding. In addition, much attention is paid to long-period infrasound (periods longer than ∼50 s), which in Europe is observed simultaneously in the troposphere and ionosphere about an hour after the arrival of the first horizontally propagating pressure pulse (Lamb wave). It is shown that the long-period infrasound propagated approximately along the shorter great circle path, similar to the previously detected pressure pulse in the troposphere. It is suggested that the infrasound propagated in the ionosphere probably due to imperfect refraction in the lower thermosphere. The observation of infrasound in the ionosphere at such large distances from the source (over 16 000 km) is rare and differs from ionospheric infrasound detected at large distances from the epicenters of strong earthquakes, because in the latter case the infrasound is generated locally by seismic waves. An unusually large traveling ionospheric disturbance (TID) observed in Europe and associated with the pressure pulse from the Hunga eruption is also discussed. Doppler sounders in East Asia, South Africa and South America did not record such a significant TID. However, TIDs were observed in East Asia around times when Lamb waves passed the magnetically conjugate points. A probable observation of wave in the mesopause region in Europe approximately 25 min after the arrival of pressure pulse in the troposphere using a 23.4 kHz signal from a transmitter 557 km away and a coincident pulse in electric field data are also discussed.

Key words: Ionosphere/atmosphere interactions; Acoustic-gravity waves; Atmospheric effects (volcano); Explosive volcanism.

1 INTRODUCTION

The submarine volcano Hunga (20.54° S, 175.38° W) explosively erupted on 15 January 2022 and generated large pressure waves propagating around the globe and detected both in the troposphere and upper atmosphere/ionosphere (Duncombe 2022; Matoza *et al.* 2022; Themens *et al.* 2022; Zhang *et al.* 2022). The most violent complex eruption sequence occurred from approximately 04:00 to 04:30 UT with maximum intensity around 4:15 UT (Matoza *et al.* 2022). During this period, an extreme amount of energy was released in the atmosphere, estimated to be (10–28) $\times$ 10^{18} J by Wright *et al.* (2022), who also provide a comparison with the estimated energy released in the atmosphere during the 1991 Pinatubo eruption ($\sim$10 $\times$ 10^{18} J) and the 1883 Krakatoa eruption ($\sim$30 $\times$ 10^{18} J). The eruption lofted volcanic material to a record-breaking height of about 55 km as shown by the stereo observations from the GOES-17 and Himawari-8 satellites (Carr *et al.* 2022).

The front of the generated atmospheric waves propagated circularly away from the volcano at speeds corresponding to Lamb waves (Lin *et al.* 2022; Wright *et al.* 2022). Lamb waves have also been detected in previous explosive volcanic eruptions, such as Krakatoa in 1883 (Pekeris 1939) and St. Helena in 1980 (Liu *et al.* 1982). This differs from atmospheric waves and ionospheric disturbances induced by seismic waves, which have been observed at large distances from the epicenters of strong earthquakes. These seismically-induced waves are generated locally by vertical motion of ground surface caused by seismic waves propagating at supersonic speeds. Consequently, they propagate nearly vertically, mostly in infrasound mode. If their period is long enough, they are only weakly attenuated and can reach ionospheric altitudes and cause disturbances that create an 'ionospheric image' of the seismic waves propagating below and can be observed by a network of dual-frequency Global Positioning Satellite System (GNSS) receivers, high-frequency Doppler radars, or ionosondes (Astafyeva *et al.* 2011; Liu *et al.* 2011; Maruyama & Shinagawa 2014; Occhipinti 2015; Liu *et al.* 2016; Chum *et al.* 2016a;a; Astafyeva 2019; Meng *et al.* 2019).

Interestingly, Lin *et al.* (2022) showed that once ionospheric disturbances associated with the 2022 Hunga eruption reached Australia, related disturbances were also almost immediately observed at a magnetically conjugate point in Japan. Traveling ionospheric disturbances (TIDs) caused by gravity waves (GWs) and observed at magnetically conjugate points with the original TIDs have already been observed and studied by modelling (Otsuka *et al.* 2004; Huba *et al.* 2015; Chou *et al.* 2022).

This paper presents observations and analysis of atmospheric waves and TID associated with the 2022 Hunga eruption in central Europe. Short-term fluctuations in the infrasound range are studied using high-resolution measurements with absolute microbarometers (Rusz *et al.* 2021; Šindelářová *et al.* 2021) and continuous Doppler sounding of the ionosphere (Laštovička & Chum 2017). Doppler observations in Argentina, South Africa, Taiwan and Japan are also discussed.

2 MEASUREMENT SETUP AND METHODS

The tropospheric measurements of atmospheric waves are based on the large aperture array of absolute microbarometers with nano-resolution referred to as WBCI (West Bohemia Czech Infrasound). The array consists of four sensors (6000-16B-IS, Paroscientific, Inc.) located in Studenec (STC), Luby (LBC), Nový Kostel (NKC) and Vackov (VAC) at mutual distances of 4–10 km in the western part of the Czech Republic and is suitable for the analysis of gravity waves and long-period infrasound (0.0033–0.4 Hz). The array configuration and coordinates can be found in (Rusz *et al.* 2021). The STC microbarometer site is also equipped with an EFM-100 electric field measurement sensor and a simple meteorological station (Rusz *et al.* 2021). The array is part of the Central and Eastern European Infrasound Network, CEEIN (Bondár *et al.* 2022).

The ionospheric perturbations are measured by multipoint and multifrequency continuous Doppler sounding system (CDSS) operating in the Czech Republic (Laštovička & Chum 2017; Chum *et al.* 2021). Signals on three different frequencies (3.59, 4.65 and 7.04 MHz) are transmitted from at least three spatially separated sites (Tx1: 50.528° N, 14.567° E; Tx2: 49.991° N, 14.538° E; Tx3: 50.648° N, 13.656° E) and received in Prague (Rx1: 50.041° N, 14.477° E) and Kašperské Hory (Rx2: 49.129° N, 13.577° E). Additional transmitters operating at 3.59 and 4.65 MHz have recently been installed at Tx4 (48.988° N, 14.777° E) and Tx5 (50.236° N, 12.373° E). The Tx4 was malfunctioning at $f = 3.59$ MHz during the Hunga event. Different frequencies are reflected from different altitudes, which can be determined from ionospheric profiles obtained each 15 min by the nearby digisonde DPS-4D located in Průhonice, about 1 km from Tx2. The Tx1 site, the Panská Ves observatory, is also equipped with an EFM-100 electric field measurement sensor, a simple meteorological station, and a very low frequency (VLF) receiver that records signals from selected European VLF transmitters at $f = 20.9$, 22.1 and 23.4 kHz located 893, 1264 and 557 km away from Panská Ves, respectively. Amplitude and phase changes of VLF signals provide information on ionization changes and ionospheric D-layer motion in the mesosphere over an altitude range of approximately 65–90 km (Silber & Price 2016; Fedorenko *et al.* 2021).

Similar single-frequency multipoint CDSSs were also installed in South Africa, Tucumán (Argentina), and Taiwan and currently operate at $f = 3.59$, 4.63 and 4.66 MHz, respectively. The exact coordinates of each transmitter and receiver can be found in (Chum *et al.* 2018b). The incomplete CDSS system, which operates on only one sounding path at $f = 4.94$ MHz, is located in France, with the receiver at the Observatoire Haute Provence (OHP), 43.93° N, 5.71° E. A new digital CDSS, based on software defined radio, was recently installed in Japan (Nakata *et al.* 2021). A map of measurement locations is shown in Fig. 1.

The propagation characteristics of waves in the GW frequency range, including the pressure pulse caused by the Lamb wave, are calculated from the observed time/phase delays between signals recorded on different sounding paths corresponding to each transmitter-receiver pair using the method described in the studies by Chum & Podolská (2018) and Chum *et al.* (2021). A 2-D version of the same method is also applied to obtain GW characteristics recorded in the troposphere by the WBCI array. To speed up calculations of spectra and propagation characteristics over long time intervals, 1-min averages of pressure calculated with high accuracy from original 50 Hz data are used. The sampling theorem is satisfied since only periods longer than about 4 min are analyzed.

Propagation characteristics of the acoustic waves in the infrasound range recorded by the WBCI array are studied using Progressive Multichannel Correlation (PMCC) method described by Le Pichon & Cansi (2003), namely the DTK-GPMCC software. The PMCC parameter settings are optimized for the WBCI array using time and frequency scaling recommendations (Garcès 2013). The spectral analysis of infrasound waves is performed keeping the

Figure 1. Map showing locations of the measurements with a zoomed-in part of Europe. Map embedded in MATLAB software (https://www.mathworks.com/) was used.

original 50 Hz sampling rate to satisfy the sampling theorem. The DTK-GPMCC software down-samples the original data to 10 Hz to speed up the calculation of propagation characteristics of the long-period infrasound in the range 0.05–0.005 Hz presented in Section 3.1.

3 RESULTS

The waves are expected to propagate from the volcano to each observation point along the individual great circle paths. However, the wind may cause some deviations from the expected trajectories. Distances and azimuths along the great circle path to Hunga volcano from the selected observation points are presented in Table 1, which also gives the pressure wave detection times and calculated celerity (effective speed of propagation from the source).

3.1 Observation in the troposphere

One-minute mean values of pressure recorded by the four sensors of the WBCI array on 15 and 16 January are shown in Fig. 2a. The absolute pressure values vary because each sensor is located at a different altitude, from 530 to 666 m above sea level (Rusz *et al.* 2021). Nevertheless, a remarkable and practically identical positive pressure pulse corresponding to the pressure wave from the Hunga eruption is observed by all sensors on 15 January around 19:27 UT (peak). The estimated celerity for the peak is around 304.4 m/s (Table 1). Note that the leading edge of the pressure pulse started to increase already at around 19:05 UT. Another significant but negative pulse associated with a wave propagating along the longer great circle path in the opposite direction to the first wave was detected on 16 January at around 01:36 UT. The calculated celerity, 304.6 m/s, is almost identical with the speed of the wave propagating along the shorter great circle path recorded on 15 January. The propagation directions are confirmed by propagation analysis. It should be noted that the pulse propagating along the longer great circle path passed through the antipodal point and interfered with waves propagating in the opposite direction. Consequently, its character has changed and differs from that of the pulse which has not yet propagated through the antipodal point.

Fig. 2 also shows the root mean square (RMS) value of pressure recorded in different frequency bands (b), averaged over all sensors, and the back-azimuths of propagating waves (c) determined from the phase delays between signals recorded by each sensor on 15 and 16 January. Fig. 2c shows that the first pressure pulse, observed on 15 January around 19:27 UT propagated roughly from the north (blue), which is consistent with the back azimuth to Hunga volcano, about 14.6°, along the shorter great circle path. On the other hand, the second pressure pulse propagated in the opposite direction, roughly from the south (red).

Figs 3a and b display in full resolution (50 Hz sampling rate) the detail of pressure recorded in Studenec (STC) from 16 to 24 UT on 15 January (interval marked by vertical dashed lines in Fig. 2a) and the spectrogram obtained from this pressure record. After the first pressure pulse, observed around 19:27 UT with an amplitude exceeding 1 hPa, infrasound waves with remarkable amplitude (∼10 Pa) were detected in the frequency range from

Table 1. Surface distance, azimuth, time of pressure pulse detection and celerity for selected points (an explosion at 4:15 UT was assumed to calculate the celerity). Values marked with (*) are estimated values for locations where pressure measurements with a time resolution of 1 min or better were not available.

Observation point	Surface distance (km)	Azimuth (°)	Time of detection (UT)	Celerity (m/s)
WBCI (center), Czech. 50.25° N, 12.44° E	16 659	14.6	19:27 (peak)	304.4
Panská Ves (PVC), Czech. 50.53° N, 14.57° E	16 586	18.3	19:23 (peak)	304.4
Oberpfaffenhofen, Germ. 48.09° N, 11.28° E	16 913	13.3	19:41 (peak)	304.4
OHP, France 43.93° N, 5.71° E	17 431	2.6	20:11 (*)	304.0 (*)
VLF (PVC-DHO) 51.86° N, 11.19° E	16 504	11.7	19:20 (*)	304.0 (*)
Chiba, Japan 35.63° N, 140.10° E	7818	135.8	11:25 (peak)	303.0
Taiwan 24.15° N, 121.28° E	8474	120.5	12:54 (peak)	307.7
Tucumán, Argentina 26.84° S, 65.23° W	10 846	242.4	14:10 (*)	303.5 (*)
Hermanus, South Africa 34.42° S, 19.22° E	13 727	163.6	16:49 (*)	303.5 (*)

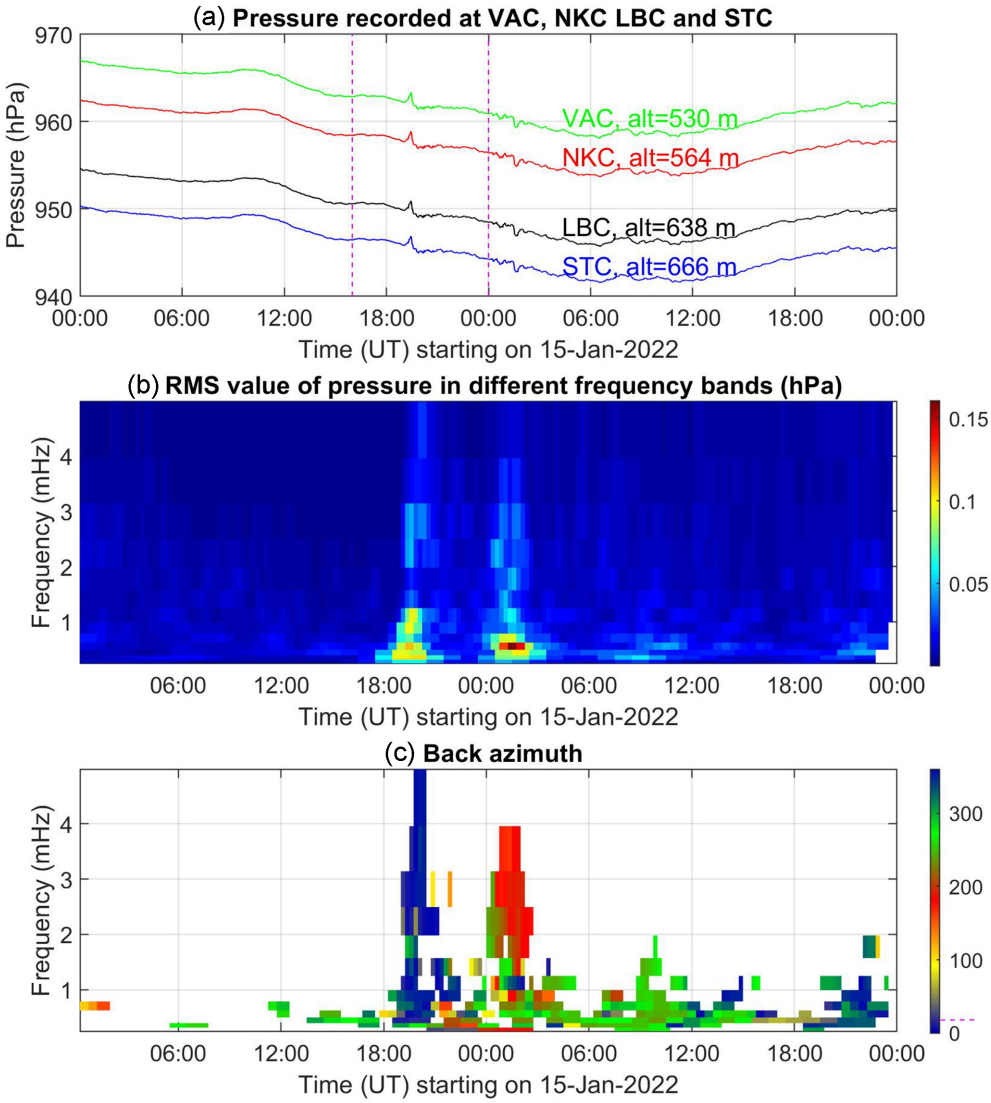

Figure 2. (a) Pressure recorded by each site of the WBCI microbarometer array in western Czechia on 15 and 16 January 2022. The vertical magenta dashed lines mark the interval shown in detail in Fig. 3. (b) Dynamic spectrum of pressure fluctuations recorded on 15 and 16 January 2022, averaged over the WBCI sensors. (c) Back-azimuth of propagating waves displayed as a function of period and time. The horizontal magenta dashed line marks on color-bar axis the back azimuth 14.6° of the shorter great circle path to Hunga volcano.

approximately 0.005 to 0.05 Hz from ∼20 to 22 UT. Coherent infrasound is observed by all sensors of the array. Results of the propagation analysis using the PMCC method for the infrasound waves observed from 20:00 to 22:00 UT (interval marked by vertical dashed lines in Fig. 3b) are displayed in Fig. 4. The infrasound waves arrived roughly from the north, their back-azimuths were similar to the back azimuth of the main pressure pulse observed approximately one hour earlier and correspond to the approximate

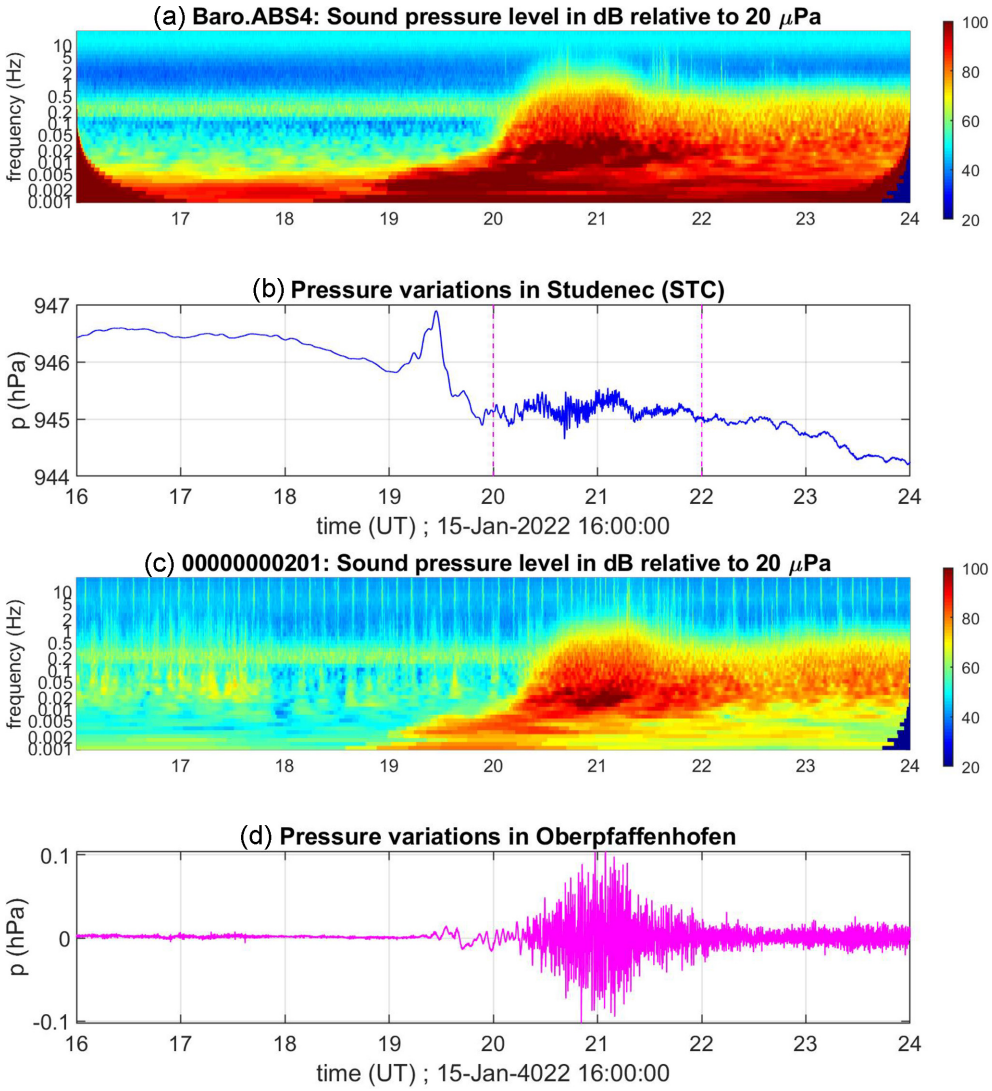

Figure 3. Spectrum (a) and pressure (b) recorded by the microbarometer in Studenec (STC) from 16:00 to 24:00 UT on 15 January 2022, and spectrum (c) and pressure variations (d) recorded by the differential microbarometer in Oberpfaffenhofen at the same time interval. The vertical magenta dashed lines in (b) mark the time interval used for the long-period infrasound propagation analysis shown in Fig. 4.

propagation along the shorter great circle path. The back-azimuth changed from approximately 12° mostly observed until about 20:30 UT to about -25° observed around 21 UT and later. The back-azimuth range appears to be wide, but the extremely long signal propagation path of ∼16 660 km (Table 1) must be taken into account. The waves propagated through different regions from sub-tropical latitudes in the southern hemisphere, across the equator and northern polar regions to the mid-latitude observation points in the northern hemisphere, with the actual propagation trajectory affected by different wind strengths and directions. Namely the polar vortex has a strong impact on the infrasound propagation over the polar regions. A number of studies have shown the key importance of winds in the middle atmosphere on infrasound propagation, including path deviations by crosswinds, effects on infrasound refraction height, and waveguide formation (e.g. Garcès *et al.* 2004; Le Pichon & Blanc 2005; Le Pichon *et al.* 2009; Evers *et al.* 2012; Assink *et al.* 2014; Blixt *et al.* 2019). Winds, together with variable vertical temperature profiles along the signal path, can contribute to the observed dispersion and time change of back-azimuths, and to the extensive time interval of infrasound arrival. The observation time interval of 20–22 UT corresponds to the celerity interval 294–261 m/s, respectively. The larger celerities are consistent with stratospheric refractions, but later arrivals of infrasound with the celerities below 280 m/s indicate refractions in the lower thermosphere (Negraru *et al.* 2010).

Infrasound of similar frequency characteristics was also detected by other ground-based stations in Europe. For example, Figs 3c and d show pressure variations and their spectral analysis, recorded in Oberpfaffenhofen (48.09° N, 11.28° E), Germany, which is approximately on the same great circle path as the WBCI array. It should be noted that the infrasound sensor, Item-prs, used in Oberpfaffenhofen is differential. Therefore, it does not measure absolute pressure and its sensitivity at frequencies in the order of 0.01 and 0.001 Hz is lower than that of the WBCI sensors. The peak of pressure pulse recorded by a nearby meteorological station occurred at ∼19:41 UT, which corresponds to a celerity of 304.4 m/s also observed by the WBCI array (Table 1).

While the Lamb wave, which is responsible for the observed pressure pulses, propagates along the shortest great circle path along the surface only horizontally, the trajectories of long-period

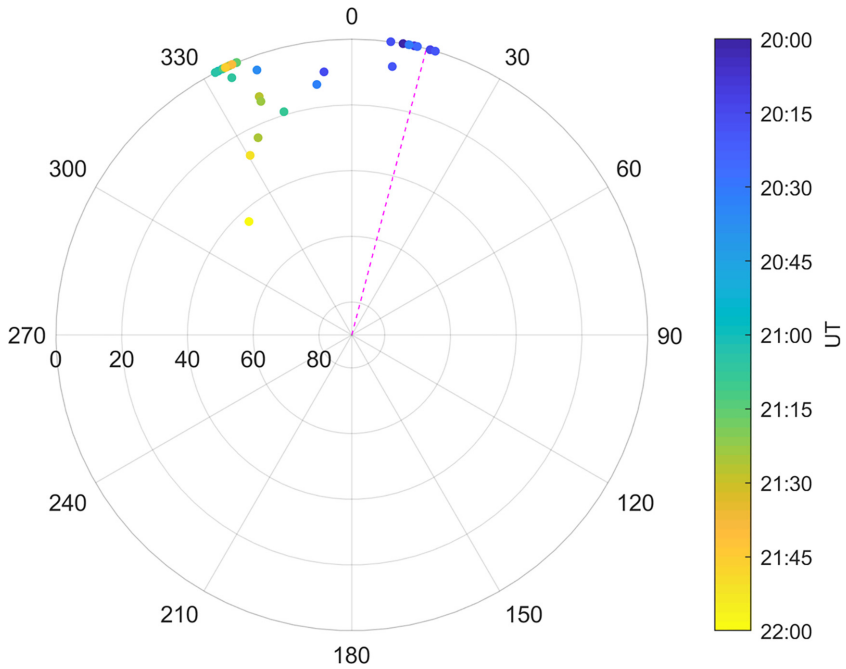

Figure 4. Propagation characteristics of infrasound waves detected by the WBCI array on 15 January 2022 from 20:00 UT to 22:00 UT. Back-azimuth by polar angle, elevation angle by radius, time of arrival is color coded. The magenta dashed line marks the back azimuth 14.6° of the shorter great circle path to Hunga volcano. See the text for more details.

infrasound are more complicated. The infrasound waves generated by the eruption propagate initially to all directions. However, only the waves propagating obliquely upwards at specific elevation angles are refracted due to the temperature and wind height profile in the stratosphere or lower thermosphere–ionosphere back to Earth's surface and reach large distances. Before reaching distances of several thousands of kilometers, they experience many such bends towards the Earth in the upper atmosphere and subsequent reflections from the Earth. Their actual path is therefore longer than that of the Lamb wave propagating only horizontally along the surface, and they are therefore detected later.

3.2 Observation in the ionosphere over the Czech Republic

Unusual signatures were observed in the ionosphere over the Czech Republic both by the digisonde and CDSS around 21 UT, >1 hr after the arrival of the first pressure pulse. Fig. 5 shows that the digisonde registered a sudden increase in the critical frequency of the F2 layer, *foF2*, around 21 UT on 15 January 2022. The *foF2* reached about 4.1 MHz at 21 UT, otherwise it was mostly below 2.9 MHz at night in the interval from ∼17:30 UT on 15 January to ∼06:30 UT on 16 January. No such sudden and temporary increase in *foF2* was observed on the surrounding days. At the same time, a downward movement of the F2 layer peak was observed—a temporary decrease in the F2 peak height, *hmF2*. The transient downward motion is consistent with the transient large positive Doppler shift observed by the CDSS. The sudden increase in *foF2* allowed the CDSS to receive signals at $f = 3.59$ MHz and $f = 4.65$ MHz reflected from the ionosphere around 21 UT, as shown in Fig. 6. We note that the CDSS received extraordinary waves at $f = 4.65$ MHz for which the critical frequency of F2 layer, *fxF2*, is about 0.66 MHz higher than for ordinary waves, $fxF2 \approx foF2 + 0.66$ (MHz), over the Czech Republic (Chum *et al.* 2016a). The estimated true reflection heights at 21:00 UT for the extraordinary waves at $f = 3.59$ MHz and $f = 4.65$ MHz are 253 and 264 km, respectively.

Remarkable large positive Doppler shift variations were observed at $f = 3.59$ and $f = 4.65$ MHz approximately from ∼20:45 to ∼21:15 UT on all sounding paths (Fig. 6). The Doppler shift at sounding frequency $f = 4.65$ MHz exceeded 4 Hz. Such large Doppler shifts are highly unusual, as documented in Fig. 7, which shows Doppler shifts (maxima of spectral intensities) recorded on the Tx1–Rx1 path in January 2022. The positive Doppler shift did not exceed ∼1.5 Hz except the large variation observed around 21 UT on 15 January. Note that the zoom of this large variation is shown in Figs 6c and d (Tx1–Rx1 corresponds to the middle trace). The gaps in Fig. 7 correspond to the intervals when no signal reflected because of the low *foF2* (usually at night) or when the Doppler shift could not be reliably determined due to a low signal to noise ratio or negligible Doppler shift (usually around noon). We stress that the observed positive variation in Doppler shift observed on 15 January around 21 UT was caused by a TID because of the time shifts between signals observed on different sounding paths. It should be noted that the $\boldsymbol{E}\mathrm{x}\boldsymbol{B}$ drift would cause virtually simultaneous changes in Doppler shift on all sounding paths. In addition, no significant changes in the geomagnetic field were observed at Budkov (49.08° N, 14.02° E) around 21 UT. The 3-D analysis (Chum & Podolska 2018; Chum *et al.* 2021) shows that the observed propagation velocity v_o, azimuth and elevation ε_0 of the TID are approximately 140 m/s, 122° and –47°, respectively. However, the estimated uncertainties are quite large, probably due to the limited observation time, namely 70 m/s, 30° and 30°. The apparent horizontal velocity, $\boldsymbol{v}_{\mathrm{HA}}$, can be calculated as $\boldsymbol{v}_{\mathrm{HA}} = \boldsymbol{v}_o/\cos(e_o)$ or obtained by 2-D analysis. The 2-D analysis provides the velocity 260 ± 80 m/s. It should be reminded that the ionospheric characteristics dramatically changed around 21 UT. Therefore, the assumed horizontal and vertical distances of the

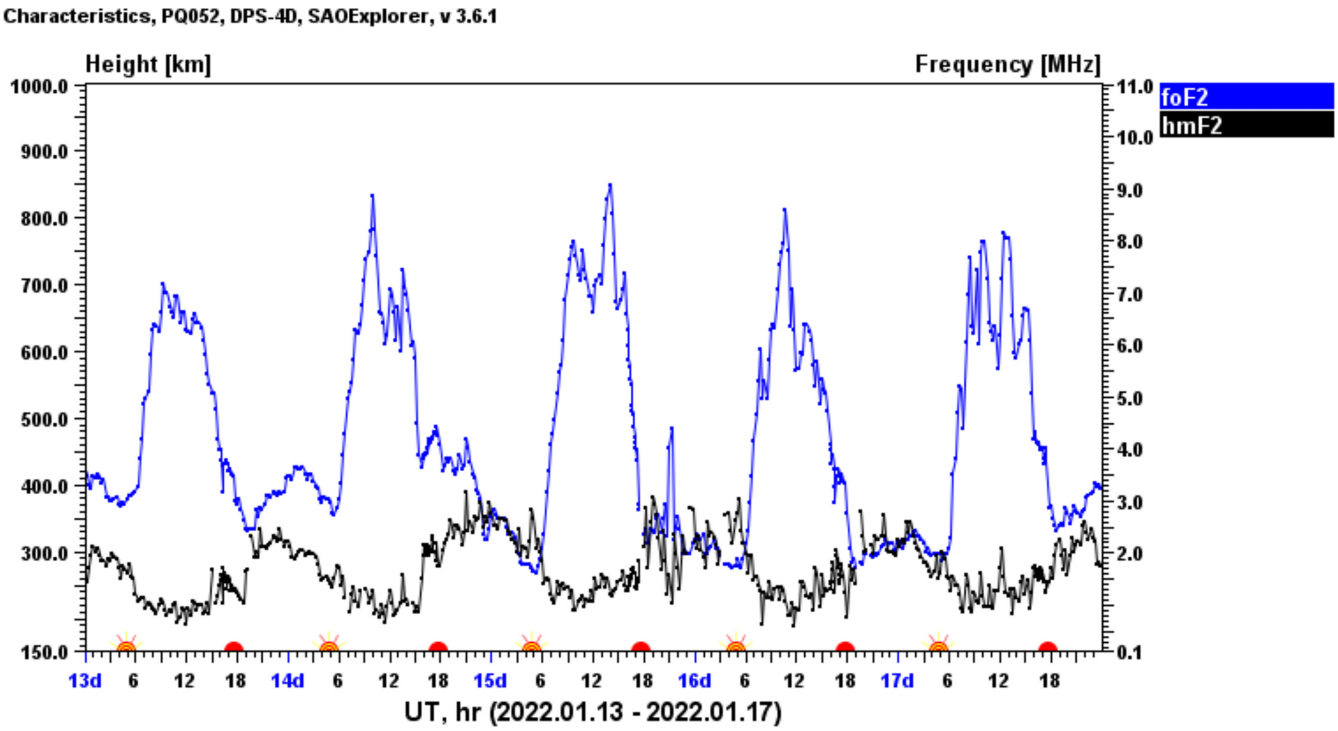

Figure 5. Critical frequency of the F2 layer *foF2* (blue) and height of the F2 layer peak *hmF2* (black) obtained from vertical ionospheric sounding in the Czech Republic, Průhonice, from 13 January 2022 00:00 UT to 18 January 2022 00:00 UT. The orange and red half-circles at the bottom of the graph correspond to the sunrise and sunset, respectively.

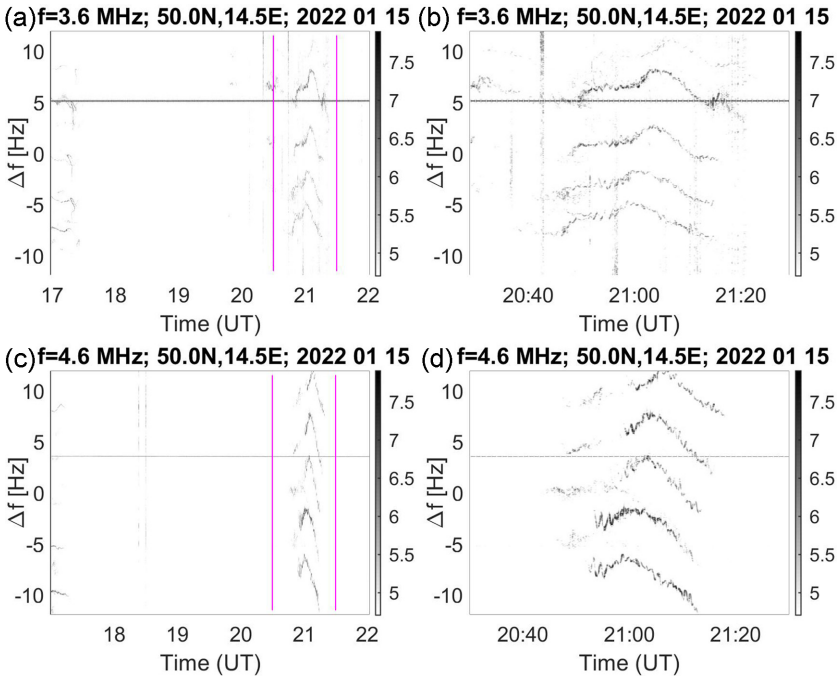

Figure 6. Doppler shift spectrogram recorded in the Czech Republic at 3.59 MHz (four sounding paths) (a) from 17 to 22 UT (b) from 20:30 to 21:30 UT and Doppler shift spectrogram recorded at 4.65 MHz (five sounding paths) (c) from 17 to 22 UT (d) from 20:30 to 21:30 UT on 15 January. The vertical magenta lines in plots (a) and (c) mark the interval displayed in plots (b) and (d).

reflection points may not be entirely correct and the obtained TID propagation characteristics may be biased.

Figs 6b and d also show that the TID observed on 15 January around 21 UT was modulated by infrasound waves. Spectral analysis shows that the infrasound power peaks at a frequency of approximately 12.5 mHz (80 s period), which corresponds to the infrasound frequencies observed on the ground at that time (Fig. 3).

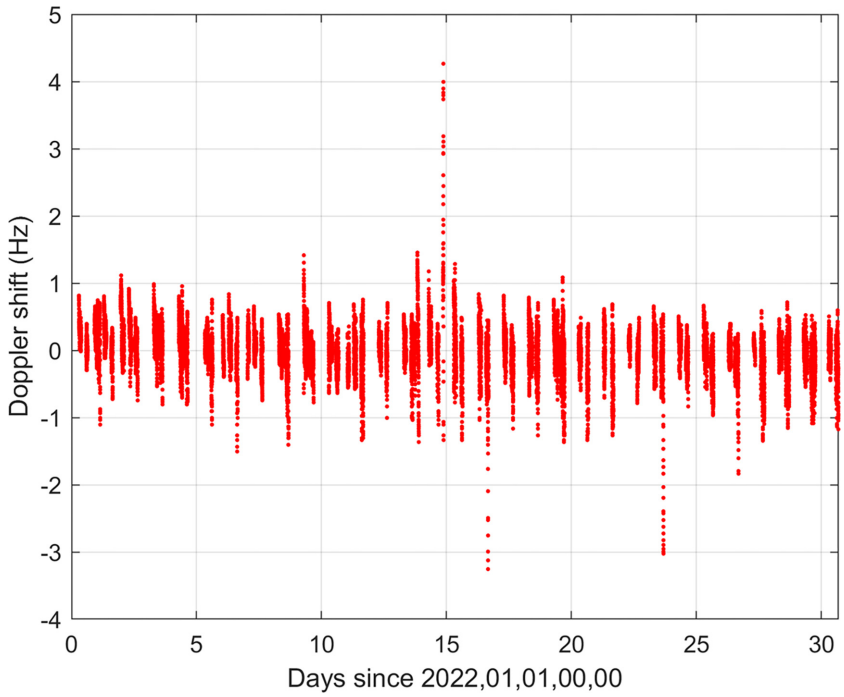

Figure 7. Doppler shifts measured at $f = 4.65$ MHz for the Tx1–Rx1 pair in January 2022.

3.3 Doppler sounding in other countries

Fig. 8 presents Doppler observations in (a) Hermanus, South Africa, (b) Observatory Haute Provence (OHP), France, (c) Taiwan, (d) Tucumán, Argentina and (e) Japan. Note that only two sounding paths were operational in South Africa and Taiwan on 15 January, and only one sounding path was installed in France. At the time of the first pressure pulse observed in the troposphere (Table 1), no significant TID was observed in any country.

Several relatively large TIDs were observed in Hermanus from ∼17:45 to ∼19:30 UT, especially the negative Doppler shifts just after 19 UT are relatively distinct. The propagation analysis is not possible owing to only two-point observation. The ionosonde located in Hermanus detected a transient increase of *foF2*. The values started to increase from about 5 MHz at 16:30 UT to almost 8 MHz at 17:25 UT and dropped again to their original values around 17:50 UT, followed by fluctuations in both *foF2* and *hmF2*. It should be noted that the *foF2* values observed in Hermanus on 15 January were much lower than those in the surrounding days, probably due to the geomagnetic storm (see Section 4).

Fig. 8b shows that the sounding signal at $f = 4.93$ MHz was only reflected over France for a very short period of time, from about 21:44 to 22:01 UT due to a sudden increase in *foF2*, similar to the Czech Republic, but about 45 min later. The extremely short observation interval and only one sounding path do not allow to investigate the TID propagation. However, infrasound was identified in the frequency range from ∼10 to ∼20 mHz with spectral peaks around 11.125 mHz (90 s) and 14.5 mHz (69 s).

Infrasound was also observed by the CDSS operating at $f = 4.63$ MHz in the ionosphere over Tucumán, Argentina, from approximately 16:15 to 16:45 UT (Fig. 8d). The highest infrasound power was in the frequency range from ∼17 to ∼20 mHz (approximately 50–60 s). The second spectral peak was also found around 14 mHz (∼70 s). It should be noted that the signal to noise ratio was relatively low in Tucumán due to high signal attenuation in the lower ionosphere during local noon. No distinct TID was detected in Tucumán. It should be noted in this respect that the observation in Tucumán was around local noon which are unfavorable conditions to detect large Doppler shifts (TIDs) at $f = 4.63$ MHz because of the reflection from the E layer (Chum *et al.* 2021).

The Doppler sounding in Taiwan, shown in Fig. 8c, did not reveal any distinct TID nor infrasound after the arrival of the tropospheric pressure pulse around 12 UT. Only diffuse, spread signal is observed. It should be noted that diffuse and oblique noise bands were often observed at this time (early night hours of local time) and were associated with equatorial spread F (Chum *et al.* 2016b), therefore the relation of spread F to waves induced by the Hunga eruption is not clear. On the other hand, a relatively large long-period TID was observed around 10 UT, followed by several short-period TIDs. A similar sequence of TIDs was also observed by a Japanese Doppler sounding system on the sounding path Chofu (JG2XA)-Sarobetsu (Nakata *et al.* 2021) as shown in Fig. 8e. These TIDs are observed around the time the ionospheric disturbances reached magnetically conjugate points in the southern hemisphere, and have also been confirmed by TEC measurements (Lin *et al.* 2022). However, it should be noted that such distinct short-period TIDs were not observed on other Doppler sounding paths in Japan.

3.4 VLF and electric field observation in central Europe

Signals from the VLF transmitters are reflected at altitudes ranging from ∼65 to ∼90 km depending on the daytime and solar activity. The amplitude of signals received at distances from ∼500 to ∼1200 km is to a great part determined by the interference of the ground wave and the wave once reflected from the ionosphere (Fedorenko *et al.* 2021). Depending on the actual reflection height, waves interfere with the same or opposite phases, which leads to an increase or decrease in the received amplitude, respectively. Similarly, depending on the actual phase shift between the ground and sky waves, an increase in the reflection height can lead to an increase or decrease in the amplitude of the received wave.

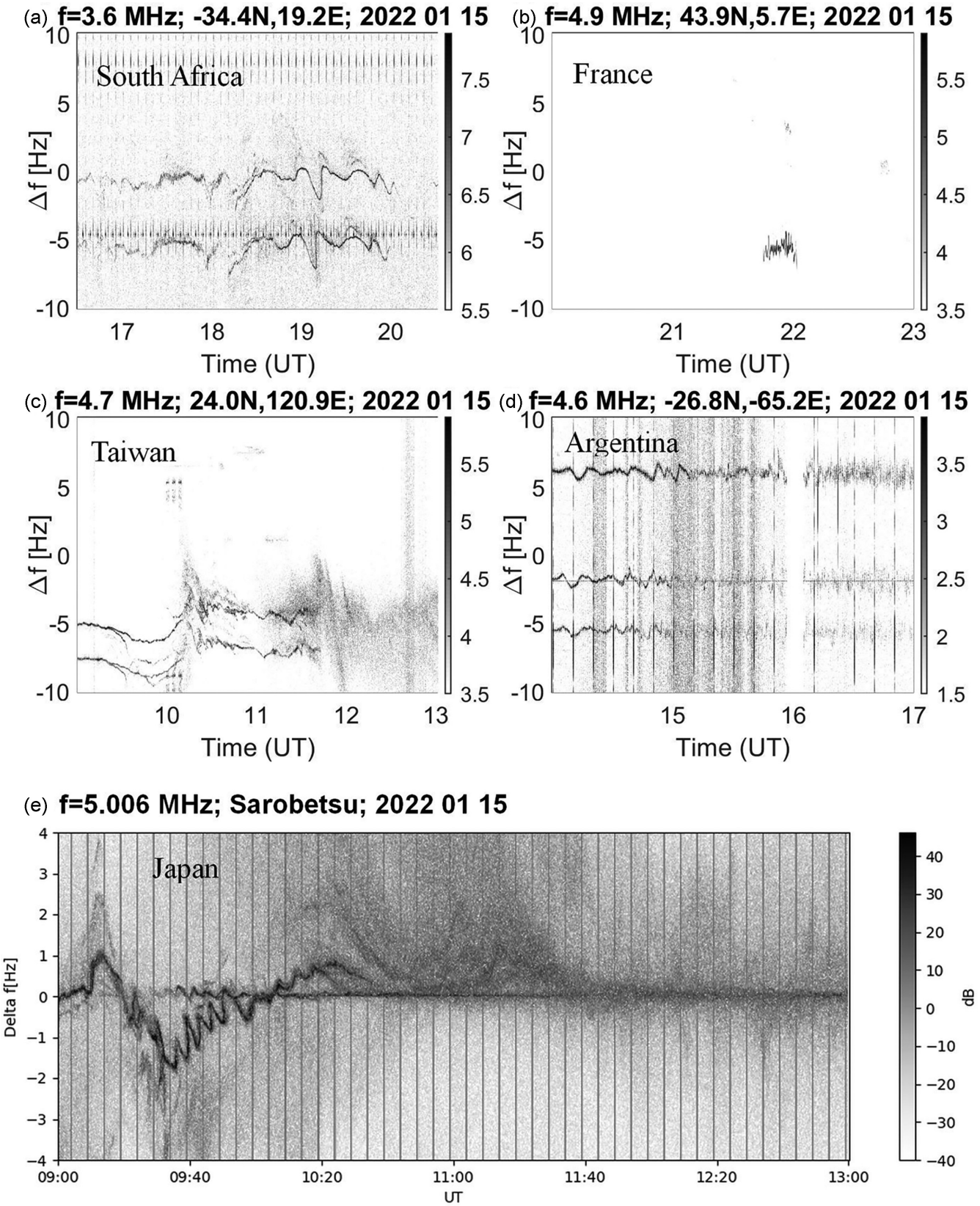

Figure 8. Doppler shift spectrogram recorded in (a) Hermanus, South Africa from 16:30 to 20:30 UT, (b) OHP, France from 20:00 to 23:00 UT, (c) Puli, Taiwan, from 09:00 to 13:00 UT, (d) Tucumán, Argentina, from 14:00 to 17:00 UT, (e) Sarobetsu, Japan, on 15 January from 09:00 to 13:00 UT. The grey scales indicate power spectral densities of the received signals in logarithmic scales.

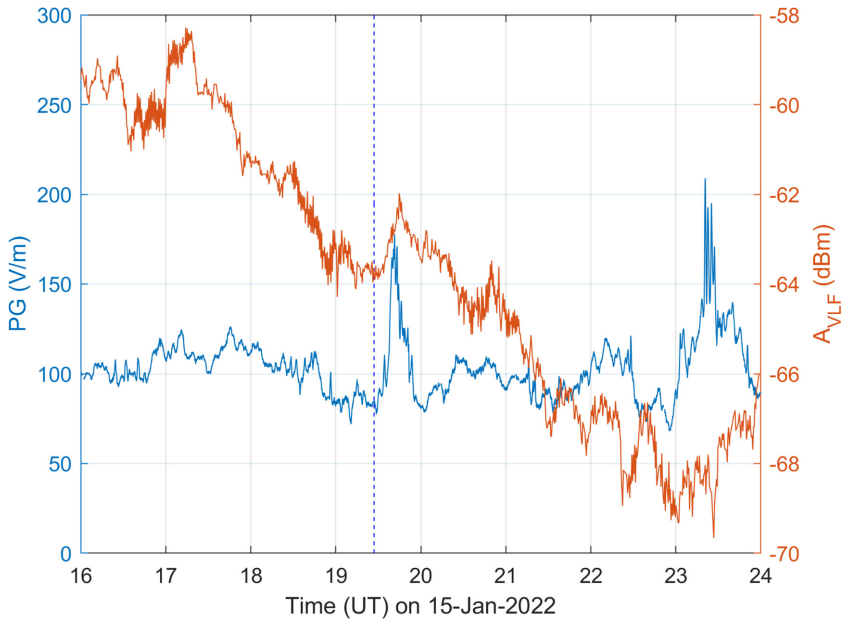

Figure 9. Amplitude of the VLF signal (red) received in Panská Ves at $f = 23.4$ kHz from DHO transmitter located in northern Germany, and PG (blue) measured in Studenec on 15 January from 16:00 to 24:00 UT. The dashed blue line indicates the time of the first pressure wave peak recorded in Studenec at 19:27 UT (Table 1).

The red line in Fig. 9 shows the amplitude of the VLF signal received in Panska Ves at $f = 23.4$ kHz from the DHO transmitter located in northern Germany at a distance of 557 km on 15 January from 16:00 to 24:00 UT. The estimated arrival time of the first pressure pulse on the ground at the midpoint between Panská Ves and DHO transmitter is 19:20 UT (Table 1), which is 7 min before the pulse arrived to Studenec site (marked by the vertical blue dashed line in Fig. 9). The VLF amplitude shows a clear positive pulse peaking around 19:45 UT that is superposed on the decreasing trend. The temporary change in the received amplitude was probably due to a transient movement of the reflection height at this time. The time of the amplitude pulse, ∼19:45 UT, is between the time of the observation of the pressure pulse on the ground and the time of detection of a significant TID (Doppler shift pulse) in the ionosphere around 21 UT. An analysis of the interference between the ground wave and the one-hop sky wave based on the approach of Fedorenko *et al.* (2021) shows that a decreasing trend in amplitude due to increasing reflection height after sunset is expected in the height range of approximately 80 to 90 km. Fig. 10a shows the simulated amplitude of the received interfering waves, normalized to the ground wave strength at a distance of 557 km from the transmitter for $f = 23.4$ kHz, and the ratio of the amplitude of the one-hop wave to the ground wave amplitude of 2 (red) and 2.5 (blue). The received amplitude decreases with increasing reflection altitude from ∼80 to 90 km. The largest sensitivity of the received amplitude to the change in reflection height is between ∼85 and ∼89 km, as shown in Fig. 10b. Thus, the transient increase in the received amplitude around 19:45 UT indicates a temporary decrease in the reflection height. Note that a temporary decrease in the reflection height was also observed in the ionosphere at altitudes above 250 km, more than 1 hour later (Figs 5 and 6). Signals received at frequencies $f = 20.9$ and 22.1 kHz from transmitters at distances 893 and 1264 km from Panská Ves, respectively, were highly disturbed, unstable and did not exhibit similar transient change of the received amplitude around 19:45 UT. It should be noted that the sensitivity of the received amplitude to changes in reflection height depends strongly on frequency and distance from the transmitter.

Fig. 9 also shows the electric field potential gradient (PG) measured in Studenec (STC) on 15 January from 16:00 to 24:00 UT (blue). The measurement of PG is collocated with one of the WBCI array microbarometers. A relatively distinct peak in the PG record is observed at 19:41 UT, approximately 14 min after the peak of the pressure pulse (Table 1), marked by vertical dashed line in Fig. 9. PG measurements are very sensitive to electrically charged regions in the clouds above, especially clouds at low altitudes, fog, and to variations in aerosol density (Nicoll *et al.* 2019). Unfortunately, we do not have direct information about cloud cover above Studenec at night. However, the measured PG values around 100 V/m are consistent with fair weather conditions (Rycroft *et al.* 2000; Nicoll *et al.* 2019). It is difficult to verify whether the transient increase in PG around 19:41 UT is due to an accidental passage of a smaller cloud over Studenec or to a pressure pulse that may have altered the electrical conductivity or charge distribution in the column between Studenec and the lower ionosphere (Haldoupis *et al.* 2017; Tacza *et al.* 2018). The PG values measured at Panska Ves show moderate fluctuations and an increasing trend throughout the day and are likely to be influenced by a thin cloud layer or fog, which is also confirmed by satellite images (https://en.sat24.com/en/).

4 DISCUSSION

The frequencies of infrasound observed in the ionosphere over the Czech Republic, France and Tucuman are consistent with the infrasound frequencies detected in the troposphere by the WBCI array and by other ground–based stations in Europe, for example in Oberpfaffenhofen, Germany (Fig. 3).

The celerity for simultaneous infrasound observations in the ionosphere and on the ground in the Czech Republic is around 276 m/s and the celerity for infrasound observations in the ionosphere over France is approximately 275 m/s. These values are consistent with

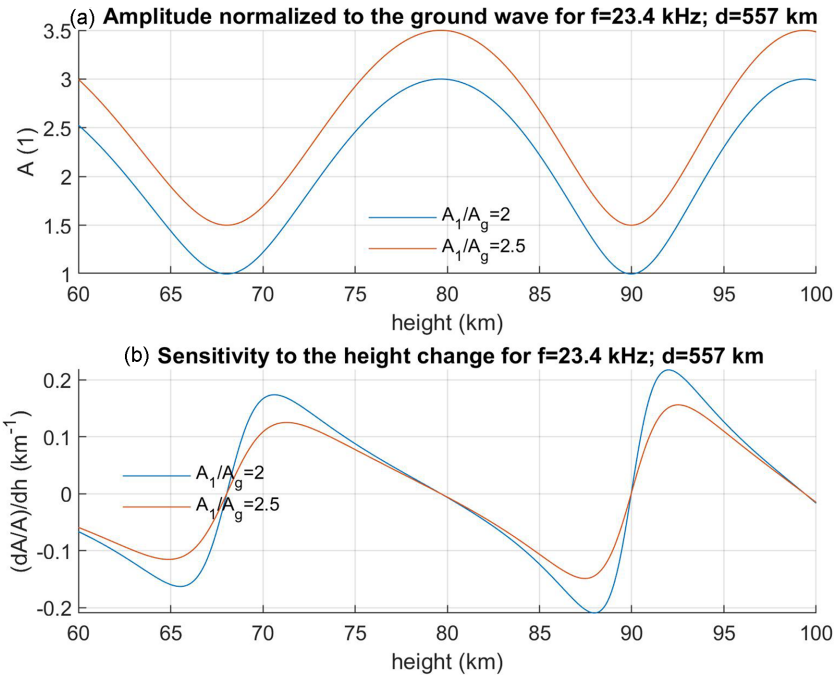

Figure 10. (a) Simulated normalized amplitude of the VLF signal for the interfering ground wave and one-hop sky wave at $f = 23.4$ kHz and 557 km distance from the transmitter as a function of the reflection height and (b) relative amplitude change due to the height change of 1 km (b) for the ratios of one-hop sky wave amplitude to the ground wave amplitude 2 (blue) and 2.5 (red).

infrasound refraction in the lower thermosphere (Negraru *et al.* 2010). Infrasound waves with the observed period, typically longer than ∼50 s, are only weakly attenuated in the atmosphere below about 150 km (Bass *et al.* 1984; Blanc 1985; Sutherland & Bass 2004; Chum *et al.* 2016a) and can propagate thousands of kilometers from the source. Such periods have usually been observed only for the most powerful eruptions, high velocity jets or oscillating plumes (Fee & Matoza 2013). It is therefore probable that some of the infrasound that propagated from Hunga eruption leaked into the ionosphere due to the imperfect thermospheric refraction. As discussed in Section 3.1, the long-period infrasound is observed after the horizontally propagating Lamb wave due to the longer trajectory caused by many Earthward bends in the upper atmosphere and subsequent reflections from the Earth. The observation of infrasound in the ionosphere at a distance of more than 16 000 km from the source is unique. It differs from seismically induced infrasound observed in the ionosphere at large distances from the earthquake epicenter, which is generated by ground surface motion due to the propagation of seismic waves roughly below the observation points in the ionosphere (Maruyama & Shinagawa 2014; Liu *et al.* 2016; Chum *et al.* 2016a;c).

No infrasound was observed by CDSSs in the ionosphere over Taiwan, Japan and Hermanus. A likely explanation is that wind field and temperature profile did not support the imperfect refraction of infrasound trajectories in the lower thermosphere and thus infrasound could not penetrate to higher altitudes at these locations. It is also possible that the wind field was not favorable for the propagation of infrasound to these locations (Garcès *et al.* 2004; Le Pichon & Blanc 2005). A possible effect of changing wind field on the ray trajectories is qualitatively discussed in Fig. 11 which shows ray tracing simulation for the case with zero background horizontal winds (Figs 11a–d), and with background winds determined by the horizontal wind model HWM14 (Drob *et al.* 2015) at the location 50° N, 15° E and 21 UT on January 2015 (Figs 11e–h). We used a ray tracing code that was originally developed to study the propagation of seismically induced infrasound to the ionosphere (Chum *et al.* 2016c). Air temperatures and composition needed to compute the sound speed were obtained from NRLMSIS model (Emmert *et al.* 2020). The attenuation along the ray trajectories is calculated using a linear approximation and an analytic model that includes classical losses due to viscosity, thermal conductivity, and losses due to rotational relaxation (Bass *et al.* 1984; Chum *et al.* 2012). The ray tracing code is only suitable for regional studies because the air characteristics only vary in the vertical direction for simplicity. The rays were started at the ground with different zenith angles α from $\alpha = 20°$ to $\alpha = 30°$ with 2° increments and are distinguished by different colors. The ray tracing simulation was stopped after 1600 s or if the rays reached the height of 300 km. A comparison of Figs 11a–d with Figs 11e–h shows that the rays launched from the ground at the same angles reach different heights. For example, the ray started with $\alpha = 26°$ (elevation 74°) reaches much higher altitudes in the case of background winds. It should be noted that the horizontal winds actually vary along the ray trajectories and especially the component of the horizontal winds parallel/antiparallel to the ray trajectory affects the refraction height. For example, imagine that to a given distance from the source along the great circle paths, only rays that previously reflected from the ground with $\alpha \geq 26°$ experienced downward refraction in the thermosphere and all the rays with initial $\alpha < 26°$ escaped to the space where they underwent strong attenuation (roughly the situation in Figs 11a–d). In other words, the rays reflected from the Earth's surface with α approximately smaller than 26° were lost for the long distance propagation. If the waves reach a region with different horizontal background winds the situation changes, and the waves with somewhat smaller initial angles α can reach the high altitudes (ionospheric F2 layer). It should also be noted that the amplitude of an infrasound wave—oscillation velocity of air particles—is a function of the altitude, wave frequency and distance over which the wave propagates at high altitudes where

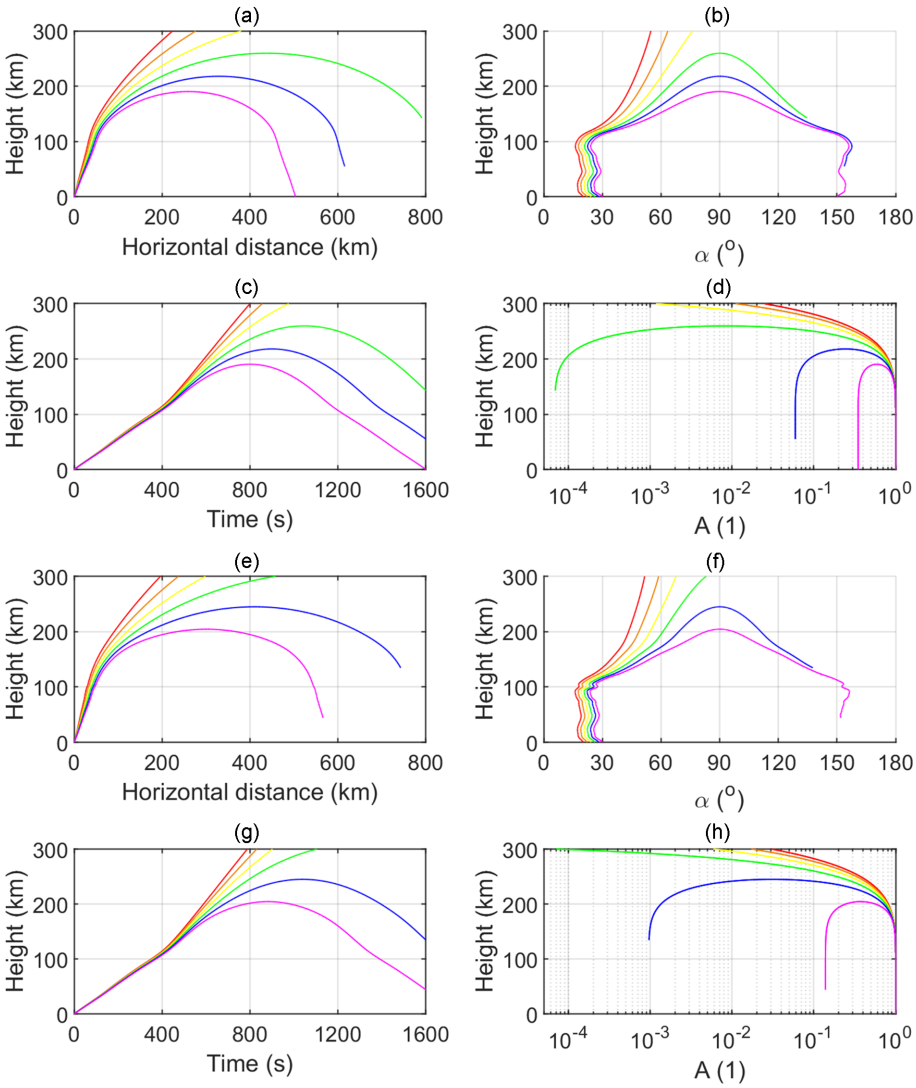

Figure 11. Ray tracing results for the infrasound waves started at height = 0 with the initial zenith angles $\alpha = 20^\circ$ (red), $\alpha = 22^\circ$ (orange), $\alpha = 24^\circ$ (yellow), $\alpha = 26^\circ$ (green), $\alpha = 28^\circ$ (blue) and $\alpha = 30^\circ$ (magenta). The plots from (a) to (d) show results obtained for zero background winds, whereas the plots from (e) to (h) display ray trajectories obtained for winds simulated by the HWM14 model. (a, e) Horizontal distances from the start. (b, f) Evolution of zenith angle α with height. (c, g) Height as a function of time. (d,h) Attenuation along the ray trajectories (relative to initial perturbations) calculated by the analytic model assuming the wave period of 80 s.

it is strongly attenuated. Figs 11d and h show attenuation along the ray trajectories. The simulation shown in Fig. 11 used a frequency of 0.0125 Hz (80 s period), which corresponds to the spectral maximum observed by the CDSS system in the Czech Republic. It is clear that infrasound of period 80 s is increasingly attenuated at altitudes above approximately 200 km. Long-range propagation is not supported at higher altitudes. It should be noted that in realistic propagation, rays with different α reflect at different locations on the Earth's surface after the refractions in the upper atmosphere. In addition, an orientation of infrasound wave vectors relative to the Earth's magnetic field could also contribute to the relatively good observing conditions in Europe. It should be reminded that CDSS detects plasma motion caused by collisions with neutral air, and plasma can freely move only along magnetic field lines at heights above ∼130 km (Rishbeth 1997; Chum *et al.* 2016a). A detailed explanation requires a global 3-D simulation of infrasound propagation using realistic wind fields and temperature profiles, and is a potential subject of future research.

The different amplitudes of TIDs and infrasound observed by continuous Doppler sounding at different locations can be partly explained by different ionospheric conditions and different reflection heights. For example, in Tucumán, Doppler signals reflected from the E layer around noon, while in the Czech Republic the reflection heights were close to the F2 peak at night. Statistical studies (Chum *et al.* 2021) show that Doppler shifts from E layer are usually negligible. The situation in East Asia was complicated by the spread F occurrence. It is an open question requiring more detailed investigation whether the occurrence of spread F could be related to the atmospheric waves generated by the Hunga eruption.

It should also be mentioned that the Hunga eruption occurred during relatively disturbed geomagnetic conditions. The Dst index reached –91 nT at 23 UT on 14 January 2022, and a recovery phase occurred on 15 January 2022. Many authors showed that large scale TIDs are often generated in auroral ovals during enhanced geomagnetic activity (Hunsucker 1982; Hocke & Schlegel 1996; Ferreira

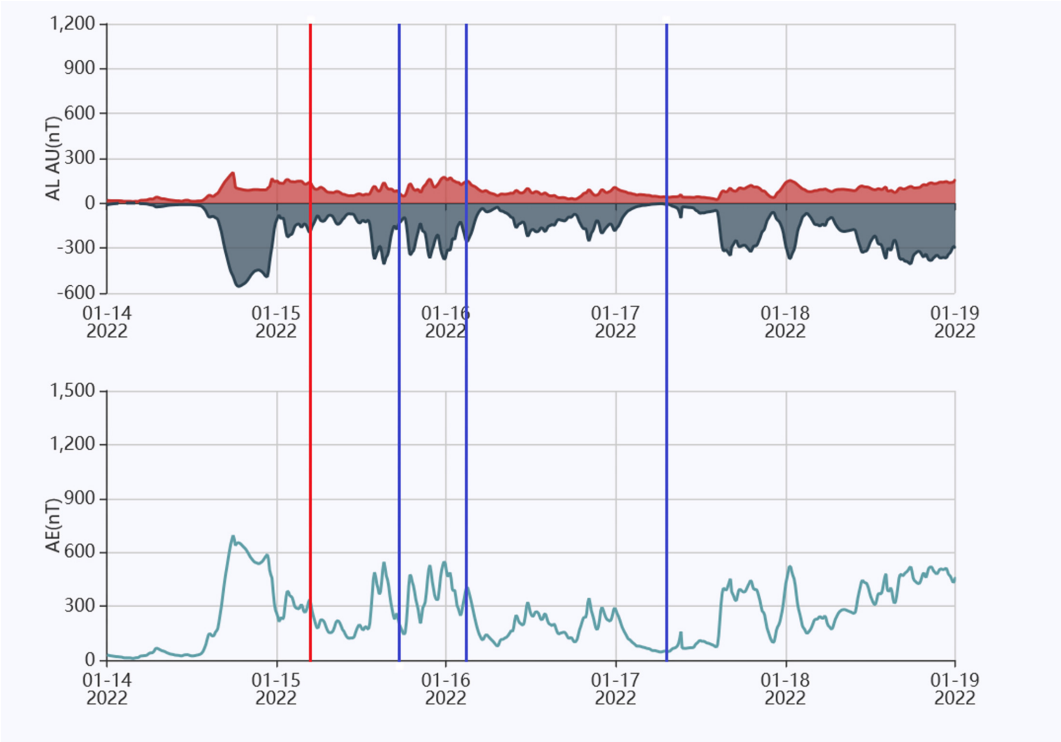

Figure 12. Auroral activity indices AL, AU and AE from 14 to 19 January and pressure pulse detections in the Czech Republic (blue lines). The Hunga eruption time is plotted by the red vertical line.

et al. 2020). Such TIDs propagated roughly equatorward at speeds between 400 and 1000 m/s and were usually observed during enhanced Auroral Electrojet (AE). The AE index is shown in Fig. 12, including its upper and lower envelopes AU and AL, respectively. Although the AE index was largest in the late hours of 14 January and several comparable local peaks occurred in the following days, the unusually large TID was only detected about 1.5 hr after the arrival of the pressure pulse in the troposphere. In addition, the rough estimate of the observed horizontal propagation velocity in the ionosphere over the Czech Republic, about 260 m/s, does not correspond to the propagation velocities usually observed for TIDs generated in the auroral oval. Therefore, it is probable that the observed TID and ionospheric anomaly (Figs 5 and 6) are related to the pressure wave generated by the Hunga eruption. In this respect, it is also useful to verify, based on the separated CDSS observations in the Czech Republic and France (Figs 6 and 8b), whether the effective propagation speed of the observed TID over Europe matches the observed speed of the pressure pulse and infrasound recorded in the troposphere. The difference between the great circle path distances from the Hunga volcano is about 800 km and the time difference between observations is approximately 45–50 min (Figs 6 and 8b). The effective propagation speed estimated from these separate observations is therefore approximately between 270 and 300 m/s, and is therefore in reasonable agreement with the celerities observed for the pressure pulse and infrasound, supporting the hypothesis that the observed TID is associated with the Hunga event. It is an open question whether the TID observed in Europe (Czech Republic and France) propagated over long distances, or whether it was gradually generated locally by atmospheric waves propagating beneath it and the TID decayed over short distances.

5 CONCLUSIONS

Tropospheric and ionospheric waves associated with the Hunga eruption were analyzed with focus on European (Czech) observations and compared with observations at other locations. The main results are as follows:

The amplitude of the first pressure pulse (Lamb wave) recorded by absolute microbarometers in the Czech Republic around 19:27 UT was higher than 1 hPa. In addition, about 40–130 min after the detection of the first pressure pulse, long-period infrasonic waves (longer than about 50 s) with an amplitude exceeding 10 Pa were observed. Similar signals were recorded by other Central European stations. The propagation directions of these waves corresponded to the approximate propagation along the shorter great circle path.

Infrasound waves with a similar period (∼50–90 s) were also detected in the ionosphere by continuous Doppler sounding in the Czech Republic at the same time interval as in the troposphere. The infrasound waves modulated the unusually large TID observed around 21 UT, which propagated at an effective speed consistent with the speed of pressure waves observed in the lower atmosphere. The infrasound is thought to have penetrated the ionosphere due to imperfect thermospheric refraction. Observations of infrasound in the ionosphere at distances greater than 16 000 km from the source are unique, and the characteristics of infrasound propagation and generation differ from observations of infrasound at large distances from the epicenter of strong earthquakes.

Observations of the ionosphere by continuous Doppler sounding in Europe differ substantially from those in East Asia, South Africa and South America, where no unusually large TIDs have been detected. On the other hand, TIDs that could be likely associated with TIDs at conjugate points were observed in East Asia. Infrasound was not observed in the ionosphere over East Asia and South Africa.

The time (∼19:45 UT) of the probable observation of a pressure pulse in the ionospheric D layer in the mesopause region by the VLF receiver at a distance of 557 km from the DHO 23.4 kHz VLF transmitter is consistent with the previous observation of the pressure pulse in the troposphere and the subsequent observation of the TID in the ionosphere.

ACKNOWLEDGMENTS

The DTK-GPMCC software was kindly provided by Commissariat à l'énergie atomique et aux énergies alternatives, Centre DAM-Île-de-France, Département Analyse, Surveillance, Environnement, Bruyères-le-Châtel, F91297 Arpajon, France. We also thank to Dr Elisabeth Blanc for initiating the installation of Doppler sounder in France. Community Coordinated Modeling Center at Goddard Space Flight Center and their publicly available simulation services (https://ccmc.gsfc.nasa.gov) are acknowledged for the HWM14 and NRLMSIS models that we used in our ray tracing code. The support by the mobility plus CONICET-22-02 project by the Czech Academy of Sciences and grant LTAUSA17100 of the Ministry of Education, Youth and Sports of the Czech Republic is acknowledged.

REFERENCES

Assink, J.D., Waxler, R., Smets, P. & Evers, L.G., 2014. Bidirectional infrasonic ducts associated with sudden stratospheric warming events. *J. Geophys. Res. Atmos.,* **119,** 1140–1153.

Astafyeva, E., Lognonne, P. & Rolland, L., 2011. First ionospheric images of the seismic fault slip on the example of the Tohoku-oki earthquake. *Geophys. Res. Lett.,* **38,** L22104, doi:10.1029/2011GL049623.

Astafyeva, E., 2019. Ionospheric detection of natural hazards. *Rev. Geophys.,* **57,** 1265–1288.

Bass, H., Sutherland, E.L.C., Piercy, J. & Evans, L., 1984. *Absorption of Sound by the Atmosphere, in Physical Acoustics,* Vol. **XVII,** Chap. 3., eds Mason, W. P. & Thurston, R. N., pp. 145–232, Academic Press, Inc.

Blanc, E., 1985. Observations in the upper atmosphere of infrasonic waves from natural or artificial sources: a summary. *Ann. Geophysicae,* **3,** 673–688.

Blixt, E.M., Nasholm, S.P., Gibbons, S.J., Evers, L.G., Charlton-Perez, A.J., Orsolini, Y.J. & Kvaerna, T., 2019. Estimating tropospheric and stratospheric winds using infrasound from explosions. *J. Acoust. Soc. Am.,* **146**(2), 973–982.

Bondár *et al.*, 2022. Central and Eastern European Infrasound Network: contribution to Infrasound Monitoring, *Geophys. J. Int.,* **230,** 565, doi:10.1093/gji/ggac066.

Carr, J.L., Horváth, A., Wu, D.L. & Friberg, M.D., 2022. Stereo plume height and motion retrievals for the record-setting Hunga Tonga-Hunga Ha'apai eruption of 15 January 2022. *Geophys. Res. Lett.,* **49,** e2022GL098131, doi:10.1029/2022GL098131.

Chou, M.-Y., Yue, J., Lin, C.C.H., Rajesh, P.K. & Pedatella, N.M., 2022. Conjugate effect of the 2011 Tohoku reflected tsunami-driven gravity waves in the ionosphere. *Geophys. Res. Lett.,* **49,** e2021GL097170, doi:10.1029/2021GL097170.

Chum, J., Hruska, F., Zednik, J. & Lastovicka, J., 2012. Ionospheric disturbances (infrasound waves) over the Czech Republic excited by the 2011 Tohoku earthquake, *J. Geophys. Res.,* **117,** A08319, doi:10.1029/2012JA017767.

Chum, J., Liu, Y.-J., Laštovička, J., Fišer, J., Mošna, Z., Baše, J. & Sun, Y.Y., 2016a. Ionospheric signatures of the April 25, 2015 Nepal earthquake and the relative role of compression and advection for Doppler sounding of infrasound in the ionosphere, *Earth Planets Space,* **68,** 24, doi:10.1186/s40623-016-0401-9.

Chum, J. *et al.*, 2016b. Spread F occurrence and drift under the crest of the equatorial ionization anomaly from continuous Doppler sounding and FORMOSAT-3/COSMIC scintillation data, *Earth Planets Space,* **68,** 56, doi:10.1186/s40623-016-0433-1.

Chum, J., Cabrera, M.A., Mošna, Z., Fagre, M., Baše, J. & Fišer, J. 2016c. Nonlinear acoustic waves in the viscous thermosphere and ionosphere above earthquake, *J. Geophys. Res. Space Phys.,* **121,** 12,126–112,137.

Chum, J. & Podolská, K. 2018. 3D analysis of GW propagation in the ionosphere, *Geophys. Res. Lett.,* **45,** 11,562–511,571.

Chum, J., Liu, J.-Y., Podolská, K. & Šindelářová, T., 2018a. Infrasound in the ionosphere from earthquakes and typhoons, *J. Atmos. Sol. Terr. Phys.,* **171,** 72–82,

Chum, J. *et al.*, 2018b. Continuous Doppler sounding of the ionosphere during solar flares, *Earth Planets Space,* **70,** 198, doi:10.1186/s40623-018-0976-4.

Chum, J., Podolská, K., Rusz, J., Baše, J. & Tedoradze, N., 2021. Statistical investigation of gravity wave characteristics in the ionosphere. *Earth Planets Space,* **73,** 60, doi:10.1186/s40623-021-01379-3.

Drob, D.P. *et al.*, 2015. An update to the Horizontal Wind Model (HWM): the quiet time thermosphere, *Earth Space Sci.,* **2,** 301–319.

Duncombe, J., 2022. The surprising reach of Tonga's giant atmospheric waves, *EOS,* **103,** doi:10.1029/2022EO220050, Published on 21 January 2022.

Emmert, J.T., Drob, D.P., Picone, J.M., Siskind, D.E., Jones, M., Jr., Mlynczak, M.G. *et al.*, 2020. NRLMSIS 2.0: a whole-atmosphere empirical model of temperature and neutral species densities. *Earth Space Sci.,* **8,** e2020EA001321, doi:10.1029/2020EA001321.

Evers, L.G., van Geyt, A.R.J., Smets, P. & Fricke, J.T., 2012. Anomalous infrasound propagation in a hot stratosphere and the existence of extremely small shadow zones, *J. Geophys. Res.,* **117,** D06120, doi:10.1029/2011JD017014.

Fedorenko, A.K., Kryuchkov, E.I., Cheremnykh, O.K., Voitsekhovska, A.D., Rapoport, Yu.G. & Klymenko, Yu.O., 2021. Analysis of acoustic-gravity waves in the mesosphere using VLF radio signal measurements, *J. Atmos. Sol. Terr. Phys.,* **219,** 105649, doi:10.1016/j.jastp.2021.105649.

Fee, D. & Matoza, R.S., 2013. An overview of volcano infrasound: from hawaiian to plinian, local to global. *J. Volc. Geotherm. Res.,* **249,** 123–139.

Ferreira, A.A., Borries, C., Xiong, C., Borges, R.A., Mielich, J. & Kouba, D., 2020. Identification of potential precursors for the occurrence of large-scale traveling ionospheric disturbances in a case study during September 2017. *J. Space Weather Space Clim.,* **10,** 32, doi:10.1051/swsc/20200 29.

Garcès, M., Willis, M., Hetzer, C., Le Pichon, A. & Drob, D., 2004. On using ocean swells for continuous infrasonic measurements of winds and temperature in the lower, middle, and upper atmosphere. *Geophys. Res. Lett.,* **31,** L19304, doi:10.1029/2004GL020696.

Garcès, M.A., 2013. On infrasound standards, part 1: time, frequency, and energy scaling, *InfraMatics,* **02,** 13–35,

Haldoupis, C., Rycroft, M., Williams, E. & Price, C., 2017. Is the "Earth-ionosphere capacitor" a valid component in the atmospheric global electric circuit, *J. Atmos. Sol. Terr. Phys.,* **164,** 127–131.

Hocke, K. & Schlegel, K., 1996. A review of atmospheric gravity waves and travelling ionospheric disturbances: 1982–1995. *Ann Geophys*., **14,** 917–940.

Huba, J.D., Drob, D.P., Wu, T.-W. & Makela, J.J., 2015. Modeling the ionospheric impact of tsunami-driven gravity waves with SAMI3: conjugate effects, *Geophys. Res. Lett.,* **42,** 5719–5726.

Hunsucker, R., 1982. Atmospheric gravity waves generated in high latitude ionosphere: a review. *Rev. Geophys,* **20,** 293–315.

Laštovička, J. & Chum, J., 2017. A review of results of the international ionospheric Doppler sounder network, *Adv. Space Res.,* **60,** 1629–1643.

Le Pichon, A. & Cansi, Y., 2003. PMCC for infrasound data processing. *InfraMatics,* **02,** 1–9.

Le Pichon, A. & Blanc, E., 2005. Probing high-altitude winds using infrasound. *J. Geophys. Res.,* **110,** D20104, doi:10.1029/2005JD006020.

Le Pichon, A., Vergoz, J., Blanc, E., Guilbert, J., Ceranna, L., Evers, L. & Brachet, N., 2009. Assessing the performance of the International Monitoring System's infrasound network: geographical coverage and temporal variabilities. *J. Geophys. Res.,* **114,** D08112, doi:10.1029/2008JD010907.

Lin, J.-T. *et al.*, 2022. Rapid conjugate appearance of the giant ionospheric lamb wave signatures in the northern hemisphere after Hunga-Tonga volcano eruptions. *Geophys. Res. Lett.,* **49,** e2022GL098222, doi:10.1029/2022GL098222.

Liu, C.H. *et al.*, 1982. Global dynamic responses of the atmosphere to the eruption of Mount 422 St. Helens on May 18, 1980, *J. Geophys. Res.,* **87**(A8), 6281–6290,

Liu, J.Y., Chen, C.H., Lin, C.H., Tsai, H.F., Chen, C.H. & Kamogawa, M., 2011. Ionospheric disturbances triggered by the 11 March 2011 M9.0 Tohoku earthquake, *J. Geophys. Res.,* **116,** A06319, 1–5, doi:10.1029/2011JA016761.

Liu, J.Y. *et al.*, 2016. The vertical propagation of disturbances triggered by seismic waves of the 11 March 2011 M9.0 Tohoku earthquake over Taiwan. *Geophys. Res. Lett.,* **43,** 1759–1765.

Maruyama, T. & Shinagawa, H., 2014. Infrasonic sounds excited by seismic waves of the 2011 Tohoku-oki earthquake as visualized in ionograms. *J. Geophys. Res. Space Phys.,* **119,** 4094–4108.

Matoza, R.S. *et al.*, 2022. Atmospheric waves and global seismoacoustic observations of the January 2022 Hunga eruption, Tonga, *Science,* **377,** 95–100.

Meng, X., Vergados, P., Komjathy, A. & Verkhoglyadova, O., 2019. Upper atmospheric responses to surface disturbances: an observational perspective. *Radio Sci.,* **54,** 1076–1098.

Nakata, H., Nozaki, K., Oki, Y. *et al.*, 2021. Software-defined radio-based HF Doppler receiving system. *Earth Planets Space,* **73,** 209, doi:10.1186/s40623-021-01547-5.

Negraru, P., Golden, P. & Herrin, E.T., 2010. Infrasound propagation in the "Zone of Silence". *Seism. Res. Lett.,* **81,** 614–624.

Nicoll, K.A. *et al.*, 2019. A global atmospheric electricity monitoring network for climate and geophysical research, *J. Atmos. Solar-Terrestrial Phys.,* **184,** 18–29.

Occhipinti, G., 2015. The seismology of the planet Mongo: the 2015 ionospheric seismology review, *Subduction Dynamics: From Mantle Flow to Mega Disasters, Geophysical Monograph 211,* eds Morra, G., Yuen, D. A., King, S. D., Lee, S.-M. & Stein, S., AGU, John Wiley & Sons, Inc.

Otsuka, Y., Shiokawa, K., Ogawa, T. & Wilkinson, P., 2004. Geomagnetic conjugate observations of medium-scale traveling ionospheric disturbances at midlatitude using all-sky airglow imagers, *Geophys. Res. Lett.,* **31,** L15803, doi:10.1029/2004GL020262.

Pekeris, C.L., 1939. The propagation of a pulse in the atmosphere, *Proc. R. Soc. London Ser. A,* **446**(A171), 434–449.

Rishbeth, H., 1997. The ionospheric E-layer and F layer dynamos—a tutorial review, *J. Atmos. Sol. Terr. Phys.,* **59,** 1873–1880.

Rusz, J., Chum, J. & Baše, J., 2021. Locating thunder source using a large-aperture micro-barometer array, *Front. Earth Sci.,* **9,** 614820, doi:10.3389/feart.2021.614820.

Rycroft, M.J., Israelsson, S. & Price, C., 2000. The global atmospheric electric circuit, solar activity and climate change. *J. Atmos. Solar-Terrestrial Phys.,* **62,** 1563–1576.

Silber, I. & Price, C., 2016. On the use of VLF narrowband measurements to study the lower ionosphere and the mesosphere-lower thermosphere, *Surv. Geophys.,* doi:10.1007/s1071 2-016-9396-9.

Sutherland, L.C & Bass, H.E., 2004. Atmospheric absorption in the atmosphere up to 160 km. *J. Acoust. Soc. Am.,* **115,** 1012–1032.

Šindelářová, T. *et al.*, 2021. Infrasound signature of the post-tropical storm Ophelia at the Central and Eastern European Infrasound Network, *J. Atmos. Sol. Terr. Phys.,* **217,** 105603, doi:10.1016/j.jastp.2021.105603.

Tacza, J., Raulin, J.-P., Mendonca, R.R.S., Makhmutov, V.S., Marun, A. & Fernandez, G., 2018. Solar effects on the atmospheric electric field during 2010–2015 at low latitudes. *J. Geophys. Res.: Atmos.,* **123,** 11,970–911,979.

Themens, D.R. *et al.*, 2022. Global propagation of ionospheric disturbances associated with the 2022 Tonga volcanic eruption. *Geophys. Res. Lett.,* **49,** e2022GL098158, doi:10.1029/2022GL098158.

Wright *et al.*, 2022. Surface-to-space atmospheric waves from Hunga Tonga–Hunga Ha'apai eruption, *Nature,* **609,** 741–746, doi:10.1002/essoar.10510674.1.

Zhang, S.-.R., Vierinen, J., Aa, E., Goncharenko, L.P., Erickson, P.J., Rideout, W., Coster, A.J. & Spicher, A., 2022. Tonga volcanic eruption induced global propagation of ionospheric disturbances via lamb waves. *Front. Astron. Space Sci.,* **9,** 871275, doi:10.3389/fspas.2022.871275.